Journal of ELECTRONIC MATERIALS, Vol. 44, No. 6, 2015
DOI: 10.1007/s11664-014-3560-0

High-Temperature Thermoelectric Properties of (1 − *x*) $SrTiO_3$ − (*x*) $La_{1/3}NbO_3$ Ceramic Solid Solution

DEEPANSHU SRIVASTAVA,[1,3] F. AZOUGH,[1] M. MOLINARI,[2] S.C. PARKER,[2] and R. FREER[1]

1.—School of Materials, University of Manchester, Manchester M13 9PL, UK. 2.—Department of Chemistry, University of Bath, Claverton Down, Bath BA2 7AY, UK. 3.—e-mail: deepanshu.srivastava@manchester.ac.uk

Ceramics based on $SrTiO_3$ are of growing interest as thermoelectric materials because of their high-temperature stability and non-toxicity. Substitution of La and Nb into the perovskite structure provides opportunities to control both the microstructure and properties. Ceramic solid solutions of $(1 - x)$ $SrTiO_3$ − (x) $La_{1/3}NbO_3$ were prepared by the mixed oxide route, using compositional steps of $x = 0.1$. Pressed pellets were sintered at temperatures of 1573 K to 1723 K in air. Addition of aliovalent ions (La^{3+}, Nb^{5+}) on the A/B sites (Sr^{2+}, Ti^{4+}) led to A-Site cation deficiency in the stoichiometric compositions and other defect structures which increased carrier concentration. A maximum ZT of 0.004 was obtained for the $x = 0.2$ stoichiometric sample, although much higher ZT values are possible by sample reduction.

Key words: $SrTiO_3$, $La_{1/3}NbO_3$, thermoelectric, cation deficiency, figure of merit

INTRODUCTION

With the rapid depletion of fossil fuels and the increasing demand for energy, renewable sources of energy and ways to increase energy efficiency are of growing importance. For over 50 years, thermoelectric generators (TEGs) have been employed which are based upon the Seebeck effect,[1] whereby a potential difference is developed across a material when its ends are held at different temperatures. TEGs can be used to generate electrical power from environments where there are temperature gradients,[2] and can be utilised to convert waste heat energy into usable electrical energy. The conversion efficiency (η) is dependent on the temperature difference (between T_{cold} and T_{hot}) and a dimensionless term, ZT, defined as the figure of merit for the material, given by Eqs. 1 and 2 below[3]:

$$\eta_{\substack{conversion\\efficiency}} = \eta_{\substack{carnot\\efficiency}} * \frac{\left(\sqrt{1+ZT}-1\right)}{\left(\sqrt{1+ZT}+\frac{T_{cold}}{T_{hot}}\right)} \quad (1)$$

$$ZT = \frac{S^2\sigma}{\kappa}T \quad (2)$$

where S is the Seebeck coefficient, σ is electrical conductivity, κ is thermal conductivity of the sample, and T is the temperature.

Traditional thermoelectric materials are frequently metallic, and include Pb-based tellurides,[4,5] and $CoSb_3$-based skutterudites.[6,7] Whilst these materials have been effective under specific environments, usually low temperature, their susceptibility to degradation at high temperature has restricted their applications. In contrast, oxide materials are stable and offer distinct stability advantages over conventional bulk materials at higher temperatures. Furthermore, oxides are generally cheaper, more environmentally safe and abundant compared to rare elements used in traditional thermoelectric materials.[8,9] The interest in oxides was spurred after the discovery of impressive thermoelectric properties in layered cobaltites, which are often p-type materials.[10,11] Over the past decade, $SrTiO_3$-based materials have emerged as one the most promising n-type materials with the highest ZT value of 0.37 following Nb doping.[12]

(Received July 15, 2014; accepted November 24, 2014; published online December 18, 2014)

Doping of $SrTiO_3$ is critical to maximise thermoelectric performance.[13–15] In this investigation, we focus on the solid solution of $SrTiO_3$ and $La_{1/3}NbO_3$. $SrTiO_3$ is known to have a stable perovskite cubic $Pm\bar{3}m$ structure,[16] while $La_{1/3}NbO_3$ has an orthorhombic $Cmmm$ structure at 300 K.[17] As La enters the perovskite A-site, and Nb enters the perovskite B-site, the addition of $La_{1/3}NbO_3$ to $SrTiO_3$ simultaneously enables site modification and generation of vacancies on both sites. The thermoelectric properties of solid solution: $Sr_{1-x}La_{x/3}Ti_{1-x}Nb_xO_3$ was investigated for values ranging between 0 and 0.3.

MATERIALS AND METHODS

The starting powders used were oxides and carbonates of Sr, Ti, La, and Nb. The powders were obtained from Sigma Aldrich (UK) ($SrCO_3$), PowerWave Technologies (UK) (La_2O_3, TiO_2), and Solvay (UK) (Nb_2O_5); all having >99.9% purity. Prior to use, the La_2O_3 was heat-treated at 1173 K for 10 h to eliminate CO_2 and moisture. The powders were mixed in appropriate molar ratios to produce the $Sr_{1-x}La_{x/3}Ti_{1-x}Nb_xO_3$ solid solutions. The samples prepared include $SrTiO_3$ (denoted as STO), and $Sr_{0.9}La_{0.034}Ti_{0.9}Nb_{0.1}O_3$, $Sr_{0.8}La_{0.067}Ti_{0.8}Nb_{0.2}O_3$, and $Sr_{0.7}La_{0.1}Ti_{0.7}Nb_{0.3}O_3$ denoted as L1, L2, L3, respectively. An excess of 0.5 wt.% of TiO_2 was added to the starting powders as sintering aid. Propan-2-ol and yttria-stabilized zirconia milling balls were added in equal weights to the powder mix and vibration milled for 24 h. The slurry was dried and calcined at 1373 K, then milled again for 24 h to reduce average particle size. The dried powders were pressed uniaxially in a hardened steel die of 20 mm diameter to produce cylindrical pellets 5 mm thick. The pellets were sintered in a Vecstar box furnace (model No. XF1) under normal pressure and oxidising conditions at 1700 K for 8 h. The densities of the sintered ceramics were determined using the Archimedes method. Circular cross-sections of individual specimens were cut using a diamond wheel, then ground and polished down to a 1-μm diamond paste followed by silica solution (OPS) ready for phase and microstructural analysis. X-ray diffraction (XRD) was carried out using a Philips X'pert diffractometer with Cu source. The pattern was recorded continuously by scanning 2θ angle from 10.0° to 85.0° with steps of size 0.030 degrees and dwell time of 10.00 s at each step. Scanning electron microscopy (SEM) was undertaken on a Phillips XL30 FEGSEM. The chemical analysis on the microstructure at 20 keV was carried out by a Rontec EDX (energy dispersive spectroscopy) system available in conjunction with XL30 FEGSEM. The SEM micrographs obtained were used to determine the average grain size by the linear intercept method.[18] The electrical conductivity and Seebeck coefficient were determined from 550 K to 1050 K using a ZEM-III (manufactured by Ulvac-Riko). The experimental setup to determine thermal diffusivity was developed in-house using a laser flash method.[19] The Cowan method[20] was used to model the compensation in heat loss and obtain temperature-dependant thermal diffusivity values of all samples in a temperature range from 300 K to 1100 K. Specific heat capacity was determined by differential scanning calorimetry (Netzsch STA 449 C) where specific heat flow into a material is measured with respect to known reference material to obtain the heat capacity of the material. For transmission electron microscopy, samples were prepared by a crushing method. The sintered disks were crushed to powder using an agate mortar and pestle. Grains of individual powders were dispersed in chloroform, dropped onto a copper grid with holey carbon film, and then dried. Atomic level resolution structural characterization was carried out using an aberration-corrected FEI TEM-STEM (80–200 keV ChemiSTEM) operating at 200 keV. High-angle annular dark field (HAADF) imaging was performed using an annular detector with an inner angle of 100 mrad and an effective outer angle of 185 mrad.

RESULTS AND DISCUSSION

The densities for all samples sintered in air were above 95% of the theoretical value. XRD analysis of the sintered $Sr_{1-x}La_{x/3}Ti_{1-x}Nb_xO_3$ solid solutions revealed that specimens having formulations based on $x > 0.3$ did not stabilise as predominantly single phase products and could not be sintered at temperatures less than 1723 K. The investigation therefore focussed on sample formulations with $0 \le x \le 0.3$. XRD spectra for the relevant specimens (STO, L1, L2 and L3) are presented in Fig. 1. All composition were indexed as a cubic perovskite structure belonging to space group $Pm\bar{3}m$. The lattice parameter increased linearly from 3.905 Å for STO, to 3.9114 Å for L1, to 3.9151 Å for L2, and to 3.919 Å for L3 composition upon La and Nb doping. The variation in lattice parameter is consistent with the Vegard's Law,[21] and the introduction of dopants of larger ionic radii;[22] lattice parameter data are shown as the inset of Fig. 1.

Typical examples of microstructures are shown as backscattered SEM micrographs in Fig. 2. The base material, STO (Fig. 2a), exhibits average grain size of 5.1 μm. For the doped samples L1, L2, L3, the increase in grain size is evident (Fig. 2b–d) with average grain sizes of 9.9 μm, 12.7 μm, and 21.1 μm, respectively. Grain growth (in L1, L2 and L3) for the same sintering conditions as for STO is also indicative of a lowering of the effective sintering temperature by doping. Another interesting feature is the optical contrast, with bright spots at the centre of few grains of L1 and L2 compositions (Fig. 2b and c). The spots are smaller than the minimum interaction volume for energy dispersive spectroscopy (EDS) to give convincing results.

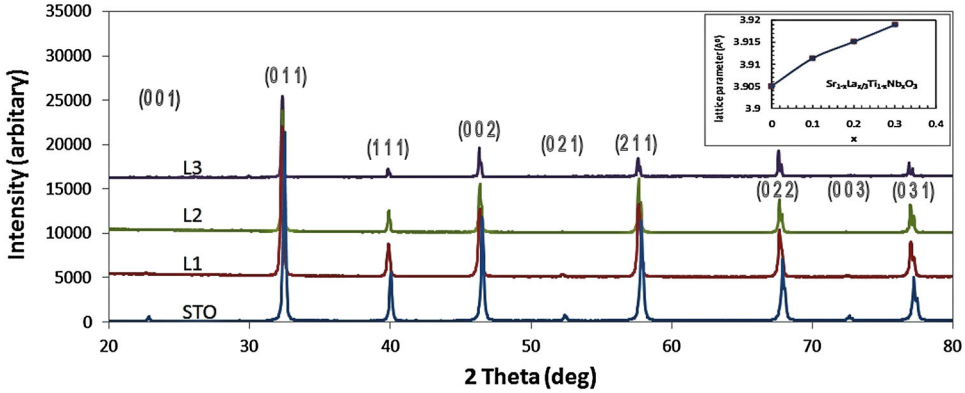

Fig. 1. X-ray diffraction spectra for compositions in the $Sr_{1-x}La_{x/3}Ti_{1-x}Nb_xO_3$ solid solution.

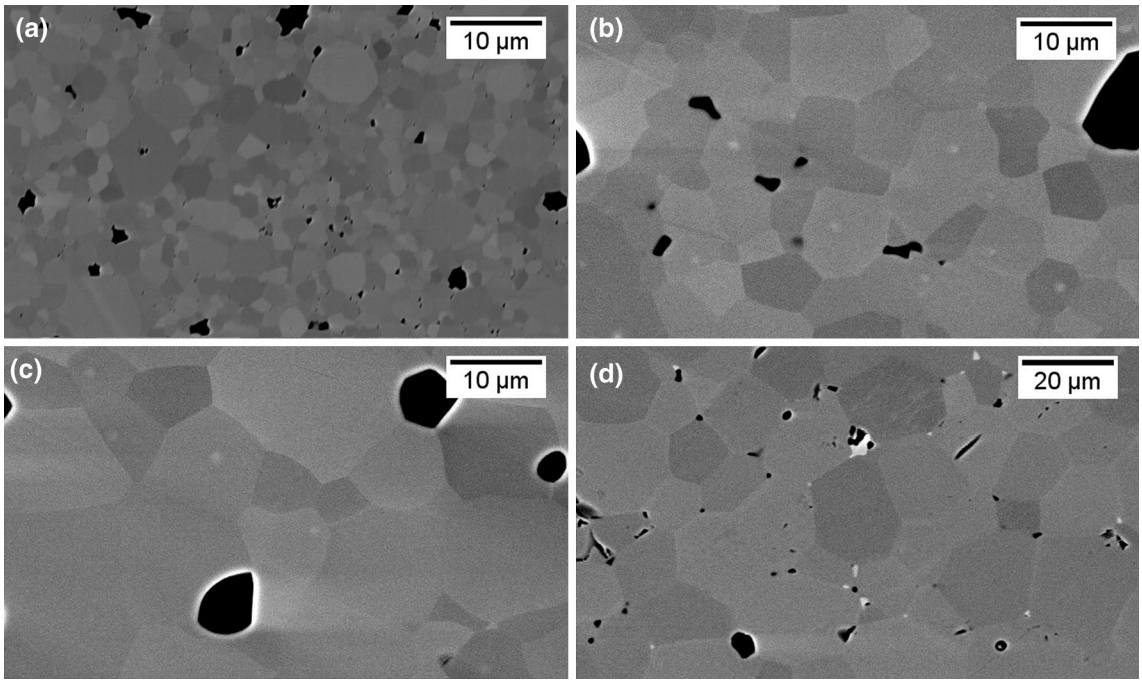

Fig. 2. Backscattered electron SEM images of samples sintered in air: (a) STO, (b) L1, (c) L2, (d) L3. Note lower magnification used in (d), to image the grain distribution and second phase.

However, the bright Z contrast suggests that there is segregation, with a composition of higher atomic weight at the core. Such 'segregation' may reflect the remnants of an intermediate phase formed during calcination. However, in terms of thermoelectric performance, such core–shell structuring and presence of additional interfaces may be beneficial if they can reduce thermal conductivity. In contrast, the L3 samples as shown in Fig. 2d did not exhibit distinct cores, but a higher atomic weight secondary phase was observed along the grain boundaries. EDX analysis confirmed the grain boundary secondary phase was rich in Nb and La.

High-resolution transmission electron microscopy was used to investigate the distribution of A-site and B-site atoms and vacancies in samples of $Sr_{0.7}La_{0.1}Ti_{0.7}Nb_{0.3}O_3$ (L3). Figure 3a shows a $\langle 1\ 0\ 0 \rangle$ orientation HAADF images for L3. In this orientation, we are effectively looking down columns of atoms, and the brightness of the spot denoting a column indicates the average atomic number of atoms in the columns; brighter means higher average atomic number[5] in the column. The very faint column shown in a circle near the top of the image indicates a vacancy-rich column. The presence of rows of A-site and B-site ions are identified near the centre of the image (Fig. 3a). Detailed intensity scans for these rows are shown in Fig. 3b and c. The uneven variation suggests that there is no evidence of ordering of La or Nb on this scale. However, there is evidence of vacancy-rich columns (such as the one

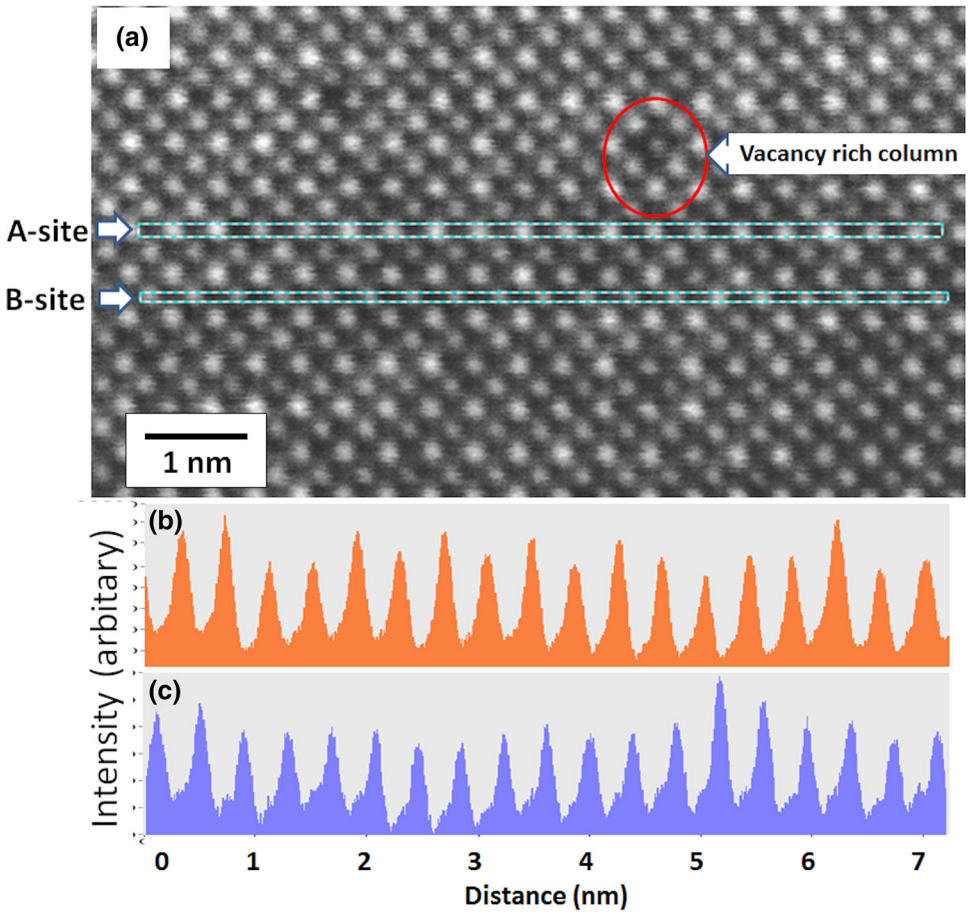

Fig. 3. (a) HAADF (Zone axis: ⟨1 0 0⟩) image for L3 showing both A-site and B-site atomic columns. The variation in the optical intensity along the rows indicates random distribution of Sr, La and vacancies in A-site and Ti and Nb in B-sites; (b) detailed intensity scan along A-sites; (c) detailed intensity scan along B-sites.

indicated in Fig. 3a), and such defect structures reflect local variations in mass which can hinder phonon propagation at higher temperatures and help to reduce thermal conductivity.

The thermoelectric properties of the samples determined at temperatures in the range 550–1050 K, are presented in Fig. 4.

There was wide variation in the resistivity of the samples (Fig. 4a). The electrical conductivity (reciprocal of resistivity) of the STO followed semiconductor behaviour reflecting the wide band gap of 3.2 eV.[23] Due to the high resistivity, data for the STO sample could not be reliably collected below 750 K. As La and Nb were substituted into the A and B sites of $SrTiO_3$, respectively, the resistivity of the doped samples at 1000 K reduced from 30 ohm-m (for STO) to 1×10^{-1} ohm-m for L1 and to 5×10^{-2} ohm-m for the L2 and L3 samples. Such changes in resistivity could be attributed to electronic structure modulation caused by La and Nb doping, as the A-site cation deficiency created by doping will affect the Ti^{4+}/Ti^{3+} ratio,[23] and will be compensated by the creation of oxygen vacancies. This mechanism would explain the lower electrical resistivity of L1/L2/L3 compared to bulk STO. Measurements of the concentration of charge carriers are needed to verify the conduction mechanism operating in the samples. Even though there is no clear trend in the reduction in resistivity for samples in $(1 - x)$ $SrTiO_3 - (x)$ $La_{1/3}NbO_3$ system for $x > 0$, it is inferred that a higher A-site deficiency will increase charge carrier concentrations. It should be noted that the increase in grain size with increase in x would marginally improve the conductivity by reducing grain boundary resistance. Indeed, the grain boundary second phases in L3 samples could have increased the resistivity against the above trend.

Undoped STO exhibits a very high Seebeck coefficient which is reduced when alloyed with $La_{1/3}NbO_3$; for example, it reduced from 1050 μV/K to 800 μV/K for L1 formulation at 1000 K (Fig. 4b). Heikes Law[24] indicates that the Seebeck coefficient is inversely proportional to the electronic charge carrier concentration. The Seebeck values for all three doped samples were negative, indicating electrons as the predominant charge carriers. Furthermore, the Seebeck coefficient did not vary

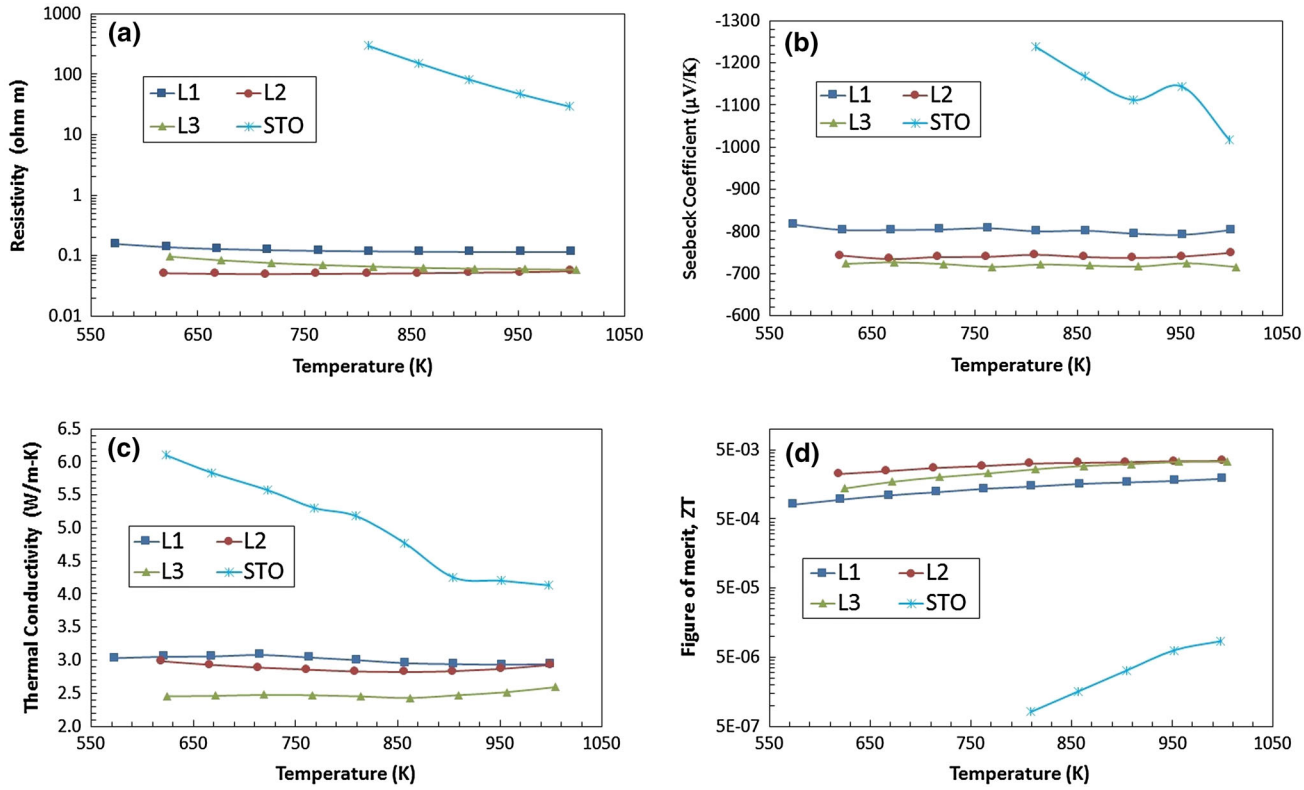

Fig. 4. Thermoelectric properties of samples in the $(1 - x)$ $SrTiO_3$ – (x) $(La_{1/3}NbO_3)$ system sintered in air. Temperature dependence of $(1 - x)$ $SrTiO_3$ – (x) $(La_{1/3}NbO_3)$ is shown as (a) resistivity, (b) Seebeck coefficient, (c) thermal conductivity and (d) figure of merit, *ZT*. Compositions STO, L1, L2, L3 corresponds to $x = 0.0, 0.1, 0.2, 0.3$, respectively.

significantly with temperature; the values followed the trends resistivity data for all the samples. From the measured electrical properties, uniform power factors, typically 5.5×10^{-6}, 1.1×10^{-5} and 7.5×10^{-6}, were deduced for L1, L2, L3 with respect to temperature. The samples reported here have not been doped with excess charge carriers (essentially stoichiometric compositions) and were sintered in oxidizing environments. Much work can be done to improve the electrical transport properties by controlled excess doping of La/Nb. The control of oxygen non-stoichiometric can also be useful in obtaining very high power factors, similar to those achieved in heavily doped oxides.[25]

The main advantage of the $(1 - x)$ $SrTiO_3$ – (x) $La_{1/3}NbO_3$ formulations is evident from the reduction of thermal conductivity (Fig. 4c). For bulk STO materials, the thermal conductivity is intrinsically high and detrimental to the thermoelectric applications. Here, the thermal conductivity of the STO samples at 600 K to 1000 K was between 6.5 W/mK and 4 W/mK, consistent with published data for polycrystalline STO samples.[26] The incremental addition of $La_{1/3}NbO_3$ had a positive effect, leading to a reduction in thermal conductivity values. This was attributed to A-site vacancies and the presence of the larger La and Nb ions in the crystal structure. These structural modifications act as scattering centres for phonon propagation at high temperatures. Moreover, the clustering of vacancies and the uneven distribution of vacancies or La/Nb ions (Fig. 3a) creates disorder in the crystal structure, assisting phonon scattering across a wider spectrum. The development of second phase segregation in sample L3 could also make a significant contribution to reducing lattice thermal conductivity, yielding the lowest thermal conductivity of 2.5 W/mK in sample L3 at 1000 K. The mean free path for phonon conduction in STO-based compositions is reported to be in the range of 0.2–10 nm which accounts for most of the heat conduction in bulk samples.[26,27] It should be possible to achieve further reduction in the overall thermal conductivity by nanostructuring the grain structure and by developing nanoinclusions at grain boundaries or nanoprecipitates within the grains.

From the thermoelectric parameters determined at 550–1050 K, the *ZT* values were determined; the highest *ZT* value of 0.004 was obtained for L2 sample as seen in Fig. 4d. The value is very low due to fact that no excess charge carrier had been added. However, it defines the best composition in studied solid solution to investigate further by controlled nanostructuring and generating excess charge carriers within the material. For example, a pilot study of L2 sintered in reducing conditions gave a *ZT* of

0.29. This investigation forms the next phase of the programme of work.

CONCLUSIONS

High density samples in the solid solution $(1 - x)$ $SrTiO_3 - (x)$ $La_{1/3}NbO_3$ system for $0 \leq x \leq 0.3$ were obtained by mixed oxide processing. The crystal structures were cubic and the lattice spacing increased with change in composition. Without excess doping of charge carriers from primary components, the La/Nb-doped L1, L2 and L3 samples exhibited improved conductivity by at least an order of 2 at 1000 K, without much reduction of Seebeck coefficient. The thermal conductivity of samples with $0 < x \leq 0.3$ was lowered by at least 25% at 1000 K for L1 sample, while the L3 sample showed lowest thermal conductivity of 2.5 W/mK at 1000 K. These improvements in properties are attributed to structural modifications, and A-site vacancies. Based on microstructural characteristics and thermoelectric properties, the L2 samples were identified as optimum amongst the samples examined. Controlled doping and tuning of oxygen vacancies improved the power factor compared to bulk STO. Use of excess doping to generate additional charge carriers is essential to generate $ZT > 0.3$. The effect of nanoinclusions and second phases in further reducing thermal conductivity will be investigated in future studies.

ACKNOWLEDGEMENTS

D.S. acknowledges support of a President's Scholarship from the University of Manchester. The SuperSTEM facilities are supported by the EPSRC.

REFERENCES

1. T.J. Seebeck, Ueber die magnetische Polarisation der Metalle und Erze durch Temperatur-Differnz. Berlin: gedruckt in der Druckerei der Königl. Akademie der Wissenschaften. 26 cm (1825).
2. T.M. Tritt, *Annu. Rev. Mater. Res.* 41, 433 (2011).
3. D.M. Rowe and C. Chemical Rubber, CRC Handbook of Thermoelectrics [electronic resource]. Boca Raton, FL: CRC Press, 1995. 1 online resource (701).
4. G.S. Nolas, in *Materials Research Society Symposium Proceedings*, November 25–30, 2012, Boston, MA, ed. by Y. Grin, D.C. Johnson, and A.J. Thompson (Warrendale: Materials Research Society, 2013), pp. xiv, 245.
5. Y. Pei, et al., *Energy Environ. Sci.* 4, 2085 (2011).
6. T. Caillat, J.P. Fleurial, and A. Borshchevsky, *J. Phys. Chem. Solids* 58, 1119 (1997).
7. G.S. Nolas, et al., *J. Appl. Phys.* 79, 4002 (1996).
8. J.W. Fergus, *J. Eur. Ceram. Soc.* 32, 525 (2012).
9. K. Koumoto, et al., *J. Am. Ceram. Soc.* 96, 1 (2013).
10. I. Terasaki, *Phys. B* 328, 63 (2003).
11. K. Koumoto, I. Terasaki, and R. Funahashi, *MRS Bull.* 31, 206 (2006).
12. K. Koumoto, et al., *Annu. Rev. Mater. Res.* 40, 363 (2010).
13. T. Okuda et al., Phys. Rev. B **63** (2001).
14. S. Ohta, et al., *J. Appl. Phys.* 97, 034106 (2005).
15. N. Wang, et al., *J. Ceram. Soc. Jpn.* 118, 1098 (2010).
16. O. Madelung, U. Rössler, and M. Schulz (ed.), $SrTiO_3$ crystal structure, lattice parameters.
17. A.N. Salak, et al., *Appl. Phys. Lett.* 93, 162903 (2008).
18. M.I. Mendelson, *J. Am. Ceram. Soc.* 52, 443 (1969).
19. W.J. Parker, et al., *J. Appl. Phys.* 32, 1679 (1961).
20. R.D. Cowan, *J. Appl. Phys.* 34, 926 (1963).
21. A.R. Denton and N.W. Ashcroft, *Phys. Rev. A* 43, 3161 (1991).
22. R.D. Shannon, *Acta Crystallogr. Sect. A* 32, 751 (1976).
23. W. Wunderlich, H. Ohta, and K. Koumoto, *Phys. B* 404, 2202 (2009).
24. R.R. Heikes and R.W. Ure, *Thermoelectricity: Science and Engineering* (New York: Interscience Publishers, 1961), p. 576.
25. C. Yu, et al., *Appl. Phys. Lett.* 92, 092118 (2008).
26. W. Yifeng, et al., *Appl. Phys. Express* 3, 031101 (2010).
27. G.G. Yadav, et al., *Nanoscale* 3, 4078 (2011).